

A Highly Sensitive Perovskite/Organic Semiconductor Heterojunction Phototransistor and Its Device Optimization Utilizing the Selective Electron Trapping Effect

Lin-Bao Luo, Guo-An Wu, Yang Gao, Lin Liang, Chao Xie,* Zhi-Xiang Zhang, Xiao-Wei Tong, Tao Wang, and Feng-Xia Liang*

Hybrid organic–inorganic perovskite materials have recently attracted attention due to their impressive physical properties and promising application in future optoelectronic devices and systems. In this study, a high-performance and broadband photodetector comprising vertically stacked Cs-doped formamidinium lead iodide (FAPbI₃) perovskite/dinaphtho[2,3-*b*:2',3'-*f*]thieno[3,2-*b*]thiophene heterojunction, which shows a high responsivity of 778 A W^{−1} and a specific detectivity of 1.04×10^{13} Jones, is reported. In addition, the photodetector displays excellent stability and broadband responsivity to illumination ranging from deep-ultraviolet to near-infrared light. It is interesting to note that doping a small amount of [6,6]-phenyl-C₆₁-butyric acid methyl ester (PCBM) into the perovskite film results in a substantial increase in responsivity, specific detectivity, and photoconductive gain. Specifically, the specific detectivity is as high as 7.96×10^{13} Jones, which is much higher than that of other devices with similar geometries. The device optimization can be ascribed to an enhanced electron–hole separation ability and increase in electron accepting sites that can selectively trap electrons in the perovskite–PCBM bulk heterojunction, according to results from the experimental analyses.

1. Introduction

Because of their excellent physical properties (e.g., appropriate direct bandgap, small exciton binding energy, long carrier


lifetime and diffusion length, and broadband light absorption), hybrid organic–inorganic perovskites have been recently regarded as a promising class of candidate materials for a range of optoelectronic applications, such as solar cells,^[1,2] light-emitting diodes,^[3,4] photodetectors,^[5–8] and lasers.^[9,10] With the rapid development in synthetic routes, various photodetectors with different device configurations have successfully exploited perovskite nanowires, nanoplates, thin films, and bulk materials.^[11–14] Compared with other counterparts, perovskite thin films can easily be prepared through facile solution-based processes and integrated in large areas with other optoelectronic systems. Therefore, they are very promising building blocks for the assembly of cost-effective optoelectronics. To date, both photodiodes and photoconductors/phototransistors assembled from perovskites have been widely explored.^[11,12]

Various studies have proven that perovskite photodiodes are highly effective in realizing high-frequency low-noise optical sensing stemming from the inherent built-in potential that suppresses dark current and enhances photocarrier separation.^[15,16] However, due to the absence of internal gain, the responsivities of these detectors are usually low (maximum values in the hundreds of mA W^{−1}), limiting their use in some special applications (e.g., weak light detection). In contrast, perovskite photoconductors/phototransistors with internal gain often enjoy a very high responsivity.^[17,18] For instance, ambipolar phototransistors made of CH₃NH₃PbI₃ thin films have achieved a peak responsivity reaching 320 A W^{−1}.^[17] Nevertheless, further performance enhancement is inevitably prohibited by the relatively poor charge carrier transport capability of perovskite thin films because of the presence of many grain boundaries and defects that act as scattering and trapping centers for photocarriers.^[19,20] One effective route is to integrate perovskite thin films with other functional materials to form hybrid photodetectors that use the photogating effect.^[11,12] In such a device, due to interfacial band alignment, one type of photocarrier excited in the perovskite can be easily injected into the functional material acting as a conducting channel, leaving another type of photocarrier trapped in the perovskite.

Prof. L.-B. Luo, G.-A. Wu, Dr. C. Xie, Z.-X. Zhang, X.-W. Tong, Dr. T. Wang
School of Electronic Science and Applied Physics
Hefei University of Technology
Hefei 230009, China
E-mail: chao.xie@hfut.edu.cn

Y. Gao
Institute of Industry and Equipment Technology
Anhui Provincial Key Laboratory of Advanced Functional Materials and Devices
Hefei University of Technology
Hefei, Anhui 230009, China

L. Liang, Dr. F.-X. Liang
School of Materials Science and Engineering
Hefei University of Technology
Hefei 230009, China
E-mail: fxliang@hfut.edu.cn

 The ORCID identification number(s) for the author(s) of this article can be found under <https://doi.org/10.1002/adom.201900272>.

DOI: 10.1002/adom.201900272

Therefore, it can allow the injected carriers to recirculate multiple times prior to recombination in the channel and provide a high gain. To date, a variety of inorganic materials, including graphene,^[21–25] 1D carbon nanotubes,^[26,27] and 2D transition metal dichalcogenides (TMDs),^[28–31] have been employed, and the resultant devices can achieve large responsivities that are several orders of magnitude higher than those of photodetectors based on pure perovskites. Despite this progress, perovskite/graphene hybrid devices normally have very large dark currents from the semimetal feature of graphene, leading to a low $I_{\text{light}}/I_{\text{dark}}$ ratio and poor signal-to-noise ratio. Detectors based on perovskite/2D TMD hybrids usually require high-quality TMD layers to realize a high photoresponse that strongly relies on a mechanical exfoliation process and makes device fabrication rather complicated and expensive. In addition, photodetectors involving 1D nanostructures and exfoliated 2D TMDs also suffer from issues in terms of unsatisfactory uniformity and poor reproducibility owing to the heterogeneity of these materials. Organic semiconductors (OSCs) have obvious advantages, including solution processability, flexibility, a light weight, and tunable optical/charge transport properties,^[32] and are ideal candidates for integration with perovskite. Various studies have revealed that OSC/perovskite hybrid photodetectors not only offer rapid transport channels for photocarriers but also retain low dark currents and sizable $I_{\text{light}}/I_{\text{dark}}$ ratios.^[33–35] Recently, by combining perovskite quantum dots (QDs) with dinaphtho[2,3-*b*:2',3'-*f*]thieno[3,2-*b*]thiophene (DNTT), Chen et al. produced a hybrid phototransistor with large responsivity and detectivity values of $1.7 \times 10^4 \text{ A W}^{-1}$ and 2.0×10^{14} Jones, respectively.^[35] Nevertheless, the response speed was relatively slow (>100 ms), probably due to slow charge transfer between adjacent QDs and/or QDs/DNTT.

In a hybrid photodetector, the change in the channel conductivity depends strongly on the net amount of charge carriers remaining in the photoactive layer.^[36] In addition to channel carrier mobility, charge separation is an essential factor for achieving high responsivity. For example, although the band alignment between perovskite and OSC in perovskite/OSC hybrid detectors can be intentionally designed to facilitate photocarrier separation at the interface of the two materials, photocarrier recombination still exists within the perovskite layer prior to electron–hole separation.^[37] Additionally, the lifetime of injected carriers is greatly reduced if the trapping time of the opposite type of carriers is very limited, which is unfavorable for a sensitive photoresponse. To this end, a feasible strategy is to introduce some charge carrier accepting sites in the perovskite layer for selective charge trapping, which has proven to be useful in some hybrid photodetectors.^[38–40] Herein, we present a hybrid photodetector based on a stacked heterojunction of a Cs-doped Cs-doped formamidinium lead iodide (FAPbI₃) perovskite and a DNTT film with a reported high charge-carrier mobility and good stability.^[41] The device exhibits a broadband photoresponse from the deep-ultraviolet (DUV) to near-infrared (NIR) regimes with high responsivity and detectivity values of 778 A W^{-1} and 1.04×10^{13} Jones, respectively. Furthermore, by incorporating [6,6]-phenyl-C61-butyric acid methyl ester (PCBM) as electron trapping centers into the perovskite layer, the responsivity and detectivity can be enhanced to $5.96 \times 10^3 \text{ A W}^{-1}$

and 7.96×10^{13} Jones, respectively. Additionally, the device possesses good ambient stability and a rapid response speed on the order of several milliseconds. The excellent photoresponse suggests the potential of the present hybrid photodetector for future high-performance air-stable optoelectronic applications.

2. Results and Discussion

Figure 1a presents the schematic device structure of the perovskite/OSC hybrid photodetector. The Cs-doped FAPbI₃ layer was prepared on a SiO₂/Si substrate by using a solution-based spin-coating approach, and the DNTT film was deposited atop the perovskite layer through thermal evaporation to form a stacked heterojunction. (Please see the Experimental Section for more details.) Considering that the concentration of Cs can directly influence the morphology/structure and consequently the optoelectronic properties of Cs-doped FAPbI₃ perovskite, three samples with different Cs doping levels ($x = 0.1, 0.15$, and 0.2) were prepared and compared in this study. Although the diffraction peaks in the X-ray diffraction (XRD) patterns for the FA_{1-x}Cs_xPbI₃ samples could be all assigned to the black phase of FAPbI₃,^[42] their field emission scanning electron microscopy (FESEM) images are obviously different, as shown in Figure S1 (Supporting Information). In the case of $x = 0.1$ or 0.2 , discontinuous perovskite films with apparent holes and defects were obtained, whereas when x was equal to 0.15 , compact and continuous films with a high quality were formed (Figure S1a–c, Supporting Information). Such a difference in morphology can lead to different capabilities for both light harvesting and charge carrier transport, which was manifested by the time-dependent photoresponse shown in Figure S1e (Supporting Information). In light of the above, FA_{0.85}Cs_{0.15}PbI₃ was employed for the assembly of the hybrid photodetectors used in this study. Figure 1b,c shows the top-view and cross-sectional FESEM images of the FA_{0.85}Cs_{0.15}PbI₃ perovskite/DNTT hybrid, from which a layer-stacked vertical heterostructure and a reasonably full coverage of the DNTT film on the perovskite layer can be clearly observed. The thicknesses of the DNTT and perovskite layers were ≈ 90 and 270 nm, respectively. As is discussed later, the reason for choosing 90 nm thick DNTT was because the DNTT with this thickness gave the highest photocurrent compared to the other thicknesses considered in this study.

The operating mechanism of the FA_{0.85}Cs_{0.15}PbI₃ perovskite/DNTT hybrid photodetector is exhibited by the energy band diagram in Figure 1d. Upon light irradiation, excitons easily dissociated into free electrons and holes owing to the small exciton binding energy (<20 meV).^[43] Holes easily diffused to the DNTT layer because the highest occupied molecular orbital (HOMO) of DNTT is slightly higher than the valence band level of perovskite, while electrons preferred to stay in the perovskite layer since the lowest unoccupied molecular orbital (LUMO) of DNTT is much higher than the conduction band level of perovskite. Consequently, electrons trapped within the perovskite acted as a local gate to effectively modulate the conductivity of the DNTT layer through capacitive coupling.^[44,45] At the same time, holes were transported and recirculated multiple times in the DNTT channel during trapping of the electrons (Figure 1e), which led to the generation of a photocurrent and was also

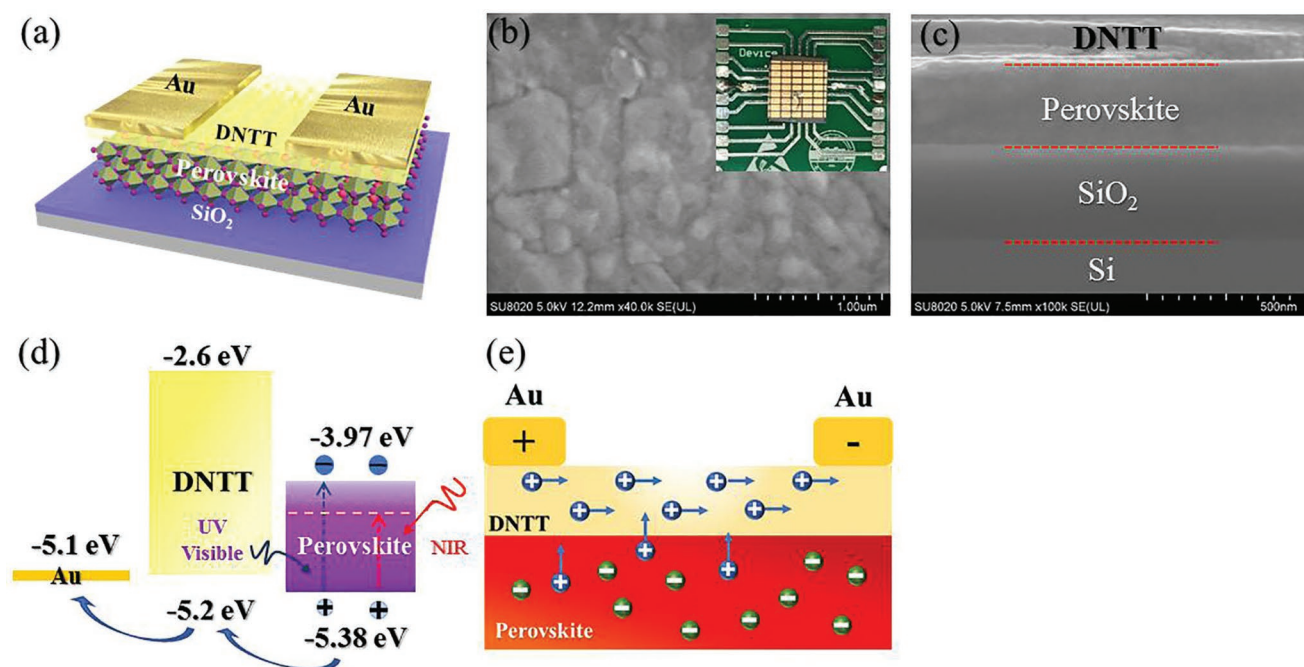


Figure 1. a) Schematic illustration of the $\text{FA}_{0.85}\text{Cs}_{0.15}\text{PbI}_3/\text{DNTT}$ hybrid photodetector. b) Top-view SEM images of $\text{FA}_{0.85}\text{Cs}_{0.15}\text{PbI}_3$ perovskite/DNTT hybrid thin film, the inset is a digital photograph of the as-prepared device. c) Cross-section SEM image of $\text{FA}_{0.85}\text{Cs}_{0.15}\text{PbI}_3$ perovskite/DNTT hybrid thin film. d) Energy band diagram and e) charge carrier distribution of the perovskite/DNTT hybrid heterojunction under light illumination.

responsible for the high gain. It is noteworthy that recombination of photoexcited electrons and holes was greatly suppressed in this unique device geometry because holes can be efficiently extracted from the perovskite layer, which increases the photocurrent.

To verify the above scenario, we then characterized the photoresponse of the hybrid photodetector. As plotted in **Figure 2a**, the device exhibited a low channel current of ≈ 20 pA at a bias voltage of 3 V in the dark. The nearly linear current–voltage (I – V) behavior indicated a good Ohmic contact between the Au electrodes and the perovskite/DNTT hybrid. Interestingly, during illumination with 450 nm light, the channel current increased dramatically to as high as ≈ 1.0 μA , suggesting ultra-high sensitivity of the hybrid photodetector. To better understand the origin of the sizable photoresponse, control devices with either DNTT or $\text{FA}_{0.85}\text{Cs}_{0.15}\text{PbI}_3$ perovskite film as the light harvesting layer were constructed and studied (Figure S2, Supporting Information). The device assembled from pure DNTT exhibited a negligible photocurrent response to light illumination, whereas the detector comprising $\text{FA}_{0.85}\text{Cs}_{0.15}\text{PbI}_3$ perovskite had a photocurrent of ≈ 0.10 μA , only one-tenth that of the hybrid photodetector under the same illumination. These results confirmed that the exceptionally large photocurrent observed in the hybrid photodetector should stem from the synergistic effect of the stacked perovskite/DNTT heterojunction rather than solely from either the perovskite or DNTT layers. In other words, the photogating effect in the perovskite/DNTT stacked heterojunction improved the photoresponse.

It should be noted that the thickness of the DNTT layer exerted a substantial influence on the photoresponse of the hybrid photodetector, as shown in Figure S3 (Supporting Information). The photocurrent increased gradually when the DNTT

thickness changed from ≈ 25 to ≈ 90 nm and then became saturated when the DNTT thickness was larger than ≈ 90 nm. This saturation was likely caused by the increased access resistance induced by carrier extraction along the thickness direction at the Au electrode contacts. For thicknesses less than ≈ 25 nm, the DNTT was too thin to form a continuous film on the perovskite layer; therefore, it led to very limited improvement of the photocurrent. The time-dependent photoresponses shown in Figure 2b revealed that the sensitivity to the incident light was highly repeatable and stable. The rise and fall edges were very steep, indicative of a fast response speed.^[46] Moreover, the photocurrent rose monotonously with increasing bias voltage, which is understandable because a larger electric field can facilitate efficient transport of photocarriers and depress their recombination activity. By carefully studying the I – V characteristics of the device under 450 nm irradiation with various light intensities (Figure 2c), one can easily observe that the photocurrent increased gradually with increasing light intensity. This phenomenon can be attributed to the increased amount of photoexcited carriers at an elevated light intensity. It is worth mentioning that even at a light intensity as weak as ≈ 46 nW cm^{-2} , the hybrid photodetector displayed a relatively large photocurrent of ≈ 7.5 nA, suggesting the potential application for weak illumination detection. The dependence of the photocurrent on the light intensity can be understood by fitting the photocurrent curve versus light intensity to a widely explored power law: $I_{\text{ph}} = P^\theta$, where I_{ph} is the net photocurrent, P is the light intensity, and θ is an empirical value reflecting the recombination of photocarriers.^[47] As shown in Figure 2d, fitting the curve in the low and high light intensity ranges gave nonideal θ values of 0.54 and 0.44, respectively, implying a strong recombination loss in the device,^[48] which can be explained by the following reasons. As

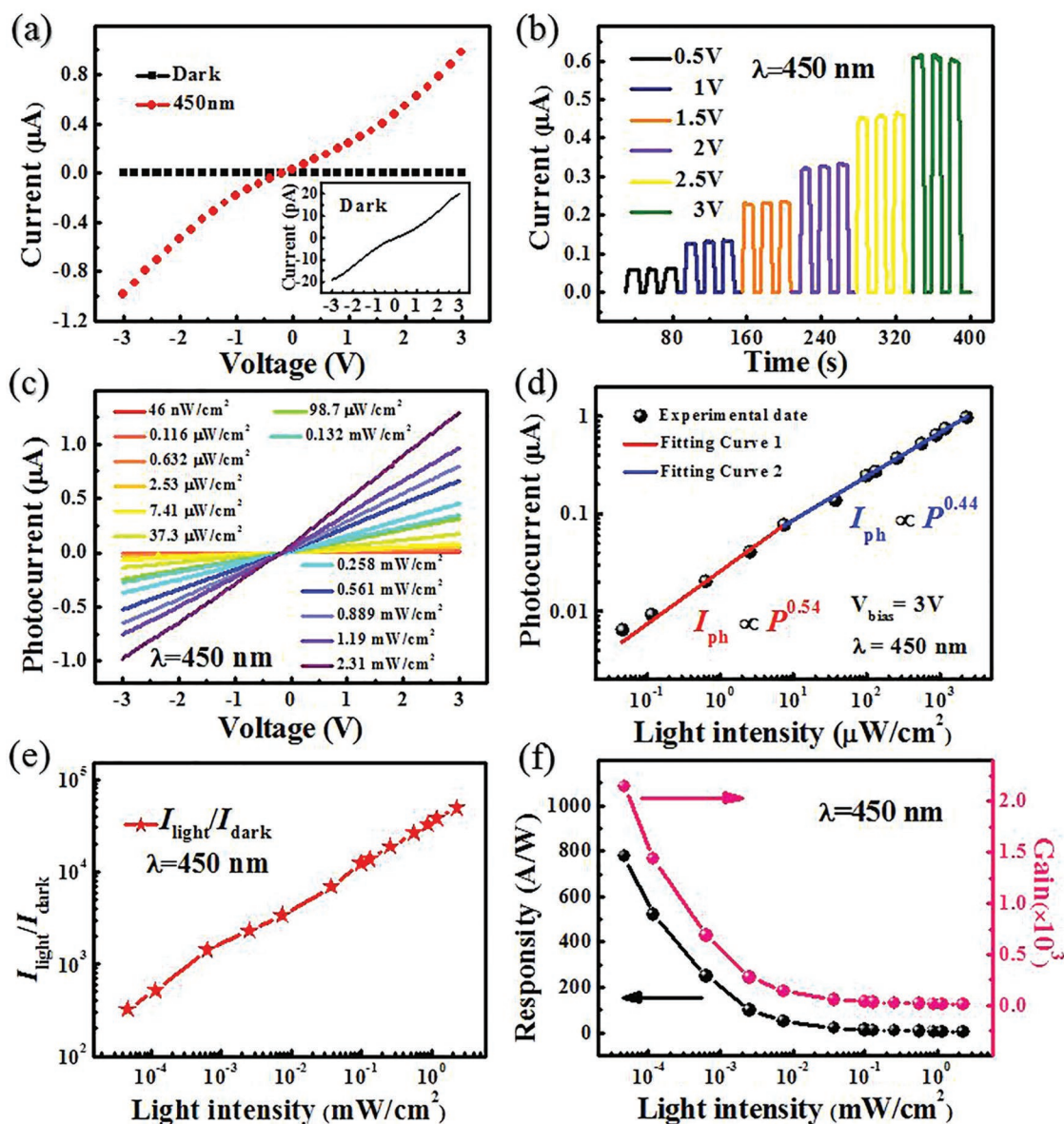


Figure 2. a) I - V characteristics of the hybrid photodetector in the dark and illuminated with 450 nm light (2.31 mW cm^{-2}), the inset is the magnified I - V curve in dark. b) Time-dependent photoresponse under 450 nm light illumination with reverse bias voltages (0.68 mW cm^{-2}). c) I - V characteristics of the device under 450 nm light illumination with various light intensities at 3 V. d) Photocurrent as a function of the incident light intensity at 3 V. e) I_{light}/I_{dark} , and f) responsivity and gain of the device as a function of incident light intensity.

discussed above, the photocarrier recombination in the perovskite layer was determined by the light intensity, and it intensified at an elevated light intensity due to an increased concentration of photocarriers.^[8] Additionally, the charge separation accumulated a reverse electric field that suppressed further injection of holes from the perovskite into the DNTT layer (Figure 1e).^[49] In addition, recombination of photocarriers may also occur at some trap states between the Fermi level and the conduction band edge of the perovskite.^[50] In addition to the photocurrent, the I_{light}/I_{dark} ratio was found to depend on the light intensity. As depicted in Figure 2e, the I_{light}/I_{dark} ratio increased gradually with increasing light intensity, and the maximum value reached 4.9×10^4 at a light intensity of 2.31 mW cm^{-2} .

Next, we calculated the responsivity (R) and gain (G), which are two crucial performance figures of merit of a photodetector. The parameter R is defined as the photocurrent produced per unit power of the incident light on the effective area of the device and is given by^[45]

$$R = \frac{I_{light} - I_{dark}}{PA} \quad (1)$$

where I_{light} , I_{dark} , P , and A are the photocurrent, the dark current, the intensity of incident light, and the effective illuminated area of the device ($A = 1.8 \times 10^{-4} \text{ cm}^2$ in this work), respectively. The parameter G is defined as the ratio between the number of

Table 1. Comparison of photoresponse parameters of our device with other reported photodetectors with similar device structures.

Device structure	R [$A W^{-1}$]	D^* [Jones]	I_{light}/I_{dark}	τ_r/τ_f	Spectral range	Ref.
FA _{0.85} CS _{0.15} PbI ₃ /DNTT	778	1.04×10^{13}	4.9×10^4	1.1/2.0 ms	UV–NIR	Our work
FA _{0.85} CS _{0.15} PbI ₃ -1% PCBM/DNTT	5.96×10^3	7.96×10^{13}	3.9×10^5	2.3/3.3 ms	UV–NIR	Our work
CsPbBr ₃ QDs/DNTT	1.7×10^4 ($V_G = -20$ V)	2×10^{14}	8.1×10^4	>100 ms	Visible	[35]
MAPbI ₃ /C8BTBT	24.8	7.7×10^{12}	2.4×10^4	4/5.8 ms	UV–NIR	[34]
MAPbI ₃ /PDPP3T	0.154	8.8×10^{10}	–	–	UV–NIR	[33]
MAPbI ₃ /MoS ₂	2.12×10^4 ($V_G = 20$ V)	1.38×10^{10}	≈ 10	10.7/6.2 s	Visible–NIR	[28]
MAPbI ₃ /WS ₂	17	2×10^{12}	1×10^5	2.5/7.5 ms	UV–visible	[30]
MAPbI ₃ /WSe ₂	110	2.2×10^{11}	10	2 s	Visible	[31]
MAPbI ₃ /graphene	180	$\approx 10^9$	–	87/540 ms	UV–visible	[21]
MAPbBr ₃ /graphene	6×10^5	–	≈ 2	750 ms	Visible	[23]

detected charge carriers and the number of incident photons, which is usually expressed as^[45]

$$G = R \frac{hc}{e\lambda} \quad (2)$$

where h , c , and λ are Planck's constant, speed of light, and wavelength of incident light, respectively. Based on the above equations, R and G were estimated to be as high as $\approx 778 A W^{-1}$ and 2.1×10^3 electrons per photon, respectively, at a low light intensity of $\approx 46 nW cm^{-2}$. This R value is higher than that of other photodetectors based on a pure perovskite film ($320 A W^{-1}$),^[17] hybrid photodetectors comprising perovskite/OSCs ($154 mA W^{-1}$ and $24.8 A W^{-1}$),^[33,34] and perovskite/2D TMDs (17 and $110 A W^{-1}$)^[30,31] described in previous reports (see Table 1). Considering that both R and G values decreased with increasing light intensity due to increased recombination activity of photocarriers (Figure 2f), we believe that both values can be further optimized given that other light sources with very weak intensity are available.

In addition, specific detectivity (D^*), which is another important performance parameter of a photodetector, was also estimated. This parameter is calculated by^[45]

$$D^* = \frac{(AB)^{1/2}}{NEP} \quad (3)$$

$$NEP = \frac{\overline{i_n^2}^{1/2}}{R} \quad (4)$$

where B is the bandwidth, NEP is the noise equivalent power, and $\overline{i_n^2}^{1/2}$ is the root-mean-square value of the noise current. By performing a Fourier transformation of the dark current, the $\overline{i_n^2}^{1/2}$ per unit bandwidth (1 Hz) was extracted to be $\approx 1 pA Hz^{-1/2}$ for our hybrid photodetector (Figure S4, Supporting Information). Therefore, the NEP was estimated to be $\approx 1.28 \times 10^{-15} W Hz^{-1/2}$, yielding a large D^* of 1.04×10^{13} Jones ($cm Hz^{1/2} W^{-1}$). This value is comparable to, or even better than, most perovskite hybrid photodetectors involving OSCs or 2D TMDs as conducting channels (see Table 1).

To explore the dependence of the photoresponse on the incident light wavelength, normalized spectral responsivity and specific detectivity at a constant light intensity were then explored. As shown in Figure 3a and Figure S5a (Supporting Information), the hybrid detector displayed a broadband photoresponse in the spectral range from DUV (250 nm) to NIR (800 nm). Figure 3b shows the time-dependent photoresponse under 254 nm, in which the hybrid detector displayed obvious sensitivity to the incident light and could be readily switched between low- and high-resistance states with good repeatability. Understandably, the observed broadband photoresponse was associated directly with the strong optical absorption of the FA_{0.85}CS_{0.15}PbI₃ perovskite/DNTT hybrid structure, as shown in Figure 3c. Figure S5b (Supporting Information) compares the spectral responsivity of photodetectors based on a perovskite/DNTT hybrid and pure perovskite film under identical measurement conditions. Apparently, for the whole wavelength spectrum, the responsivity of the hybrid photodetector surpassed that of the pure perovskite-based device by more than one order of magnitude. The above results demonstrate that the photogating effect in the stacked heterojunction substantially promoted the photoresponse in the broadband wavelength spectral region. Although the absorption obviously declined at long wavelengths (>800 nm), the hybrid device still exhibited decent sensitivity in this region. For example, when 850 nm light illumination was chosen to shine the device, an obvious sensitivity with good reproducibility was still observed (Figure 3d). Such an NIR photoresponse beyond the intrinsic optical absorption limit of FA_{0.85}CS_{0.15}PbI₃ perovskite (≈ 800 nm) was likely due to photocarriers that were excited from the valence band to the defects states within the perovskite bandgap (Figure 1d).^[8,51]

Along with high responsivity and broadband photoresponse, the present hybrid detector also had a relatively fast response speed. Figure 4a schematically illustrates the setup for measuring the response speed, where the pulsed light signal was produced by a 450 nm laser diode driven by a signal generator, and a digital oscilloscope connected in parallel in the circuit was used to monitor the variation of the photoresponse. When light with frequencies ranging from 10, 50 to 200 Hz were shined on the device, it was readily switched on and off with good reproducibility. By calculating the response speed from an

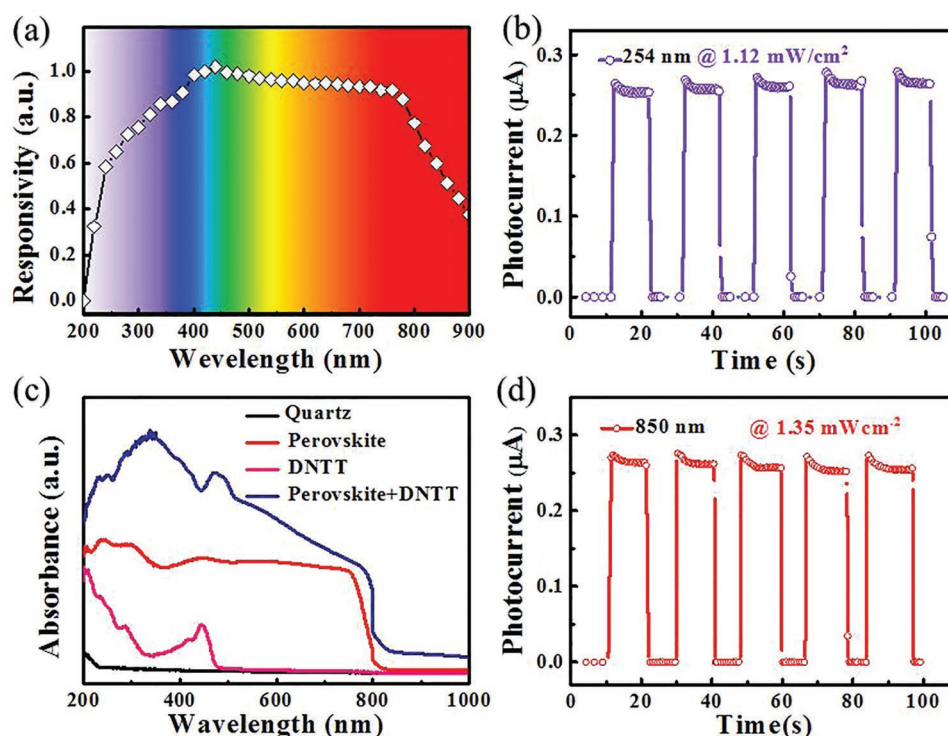


Figure 3. a) Spectral responsivity of FA_{0.85}Cs_{0.15}PbI₃ perovskite/DNTT hybrid photodetector. b) Time-dependent photoresponse of the device to repeatable on/off light with wavelengths of 254 nm. c) Absorption spectrum of the FA_{0.85}Cs_{0.15}PbI₃ film, DNTT film, and FA_{0.85}Cs_{0.15}PbI₃/DNTT hybrid film on quartz substrate. d) Time-dependent photoresponse of the device to periodic on/off illumination at wavelengths of 850 nm.

individual magnified response curve at 200 Hz (Figure 4e),^[52] the τ_r (duration required for the photoresponse to increase from 10 to 90%) and τ_f (duration required for the photoresponse to

decrease from 90 to 10%) were estimated to be 1.1 and 2.0 ms, respectively, which are very fast considering the fact that there is a trade-off between the gain and response speed, and hybrid

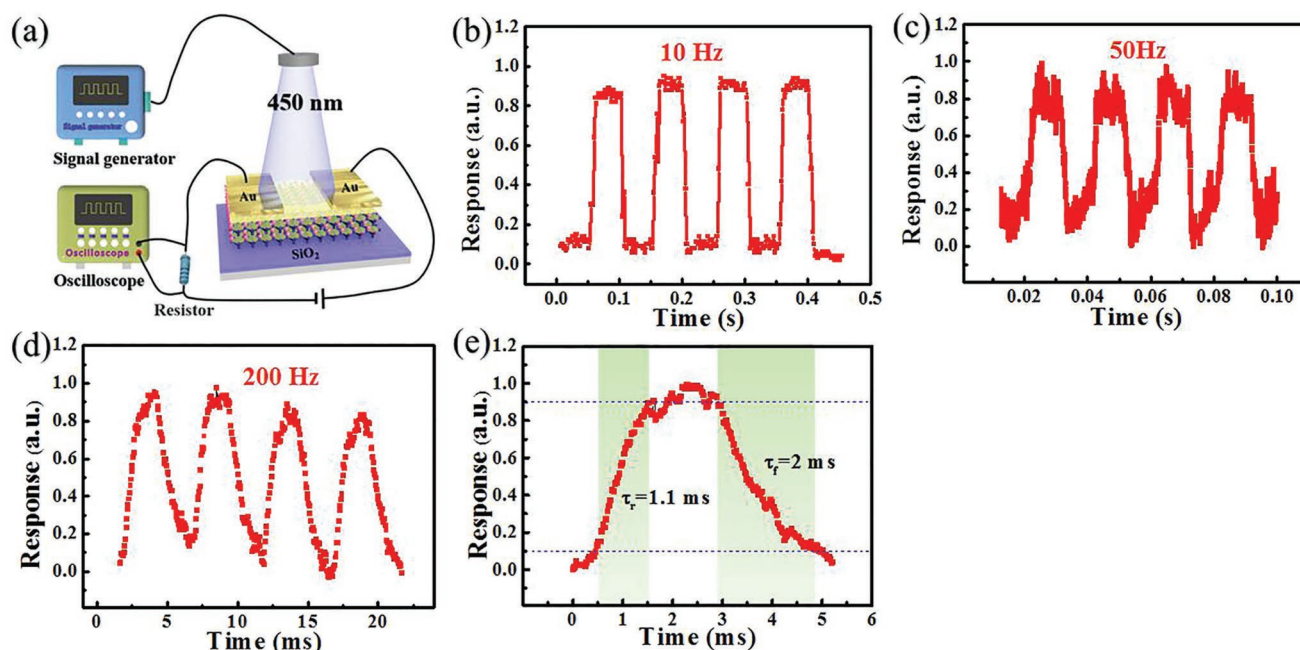


Figure 4. a) Schematic illustration of the setup for response speed measurement. b–d) Photoresponse of the device under 450 nm light illumination with a frequency of 10, 50, and 200 Hz, respectively, the light intensity is 1.27 mW cm⁻². e) Single magnified photoresponse curve at 200 Hz for estimating both rise/fall times.

photodetectors with high responsivity are often characterized by a very slow response speed. It even constitutes the fastest device among perovskite/OSCs, perovskite/graphene, and perovskite/2D TMD hybrid photodetectors reported to date (Table 1), suggesting promising applications for high-speed optoelectronic devices and systems. This rapid response speed could be attributed to the following two reasons. First, due to the vertical heterostructure of the double-layer thin films, the photoexcited holes generated in the perovskite can be quickly transported to the DNTT layer. This is quite different from the situation in the perovskite QDs/DNTT heterostructure reported previously, where photocarriers needed to transfer between adjacent QDs before arriving at the DNTT layer.^[35] The presence of organic ligands around the QDs may also influence the charge transfer process. In addition, in comparison to those of other perovskite films with similar carrier lifetimes, Cs-doped FAPbI₃ perovskite films possess relatively longer carrier diffusion lengths and lower trap densities,^[42] which would reduce the probability of trapping/detrapping photocarriers during their transfer between the perovskite and DNTT and is therefore helpful for fast response speeds.

We further characterized the repeatability and air stability of the hybrid photodetector, which are critical parameters for practical application. Figure 5a shows the time-dependent photoresponse under continuously switched 450 nm irradiation over 1000 cycles of operation. Remarkably, the photoresponse remained almost unchanged with slight fluctuations in photocurrent, most likely caused by the variation in incident

light intensity for each cycle, implying excellent repeatability and long-term durability. Figure 5b,c summarizes the evolution of both the dark current and photocurrent under illumination with 254, 450, and 850 nm light in ambient conditions (relative humidity: 45–55%) without any encapsulation and protection for different durations (30 and 90 d). The dark current remained nearly identical, whereas the photocurrent suffered from a degree of degradation after storage for 90 d. Careful analysis found that the photocurrent only decreased by 5–10% after storage for 30 d and 10–25% after storage for 90 d (the percentage is dependent on the incident wavelength). Such good device stability was attributed to the compact DNTT layer that can prevent moisture ingress into the perovskite (although the degradation of perovskite cannot be avoided, as shown in Figure S6, Supporting Information).^[53]

As mentioned above, the recombination of the photocarriers before the extraction of holes near the perovskite/DNTT interface is harmful to the photoresponse of the hybrid photodetector. One possible solution to this issue is to import electron accepting sites to selectively trap photoexcited electrons, which can avoid carrier recombination within the perovskite active layer and therefore improve the device performance. In light of this, [6,6]-phenyl-C₆₁-butyric acid methyl ester (PCBM), a typical electron acceptor that has been widely used in perovskite solar cells was incorporated into the perovskite layer to form bulk heterojunctions (BHJs).^[54,55] Figure 6a shows the energy band diagram of perovskite-PCBM BHJ/DNTT hybrid heterostructure, where it can be seen that once the PCBM was doped into

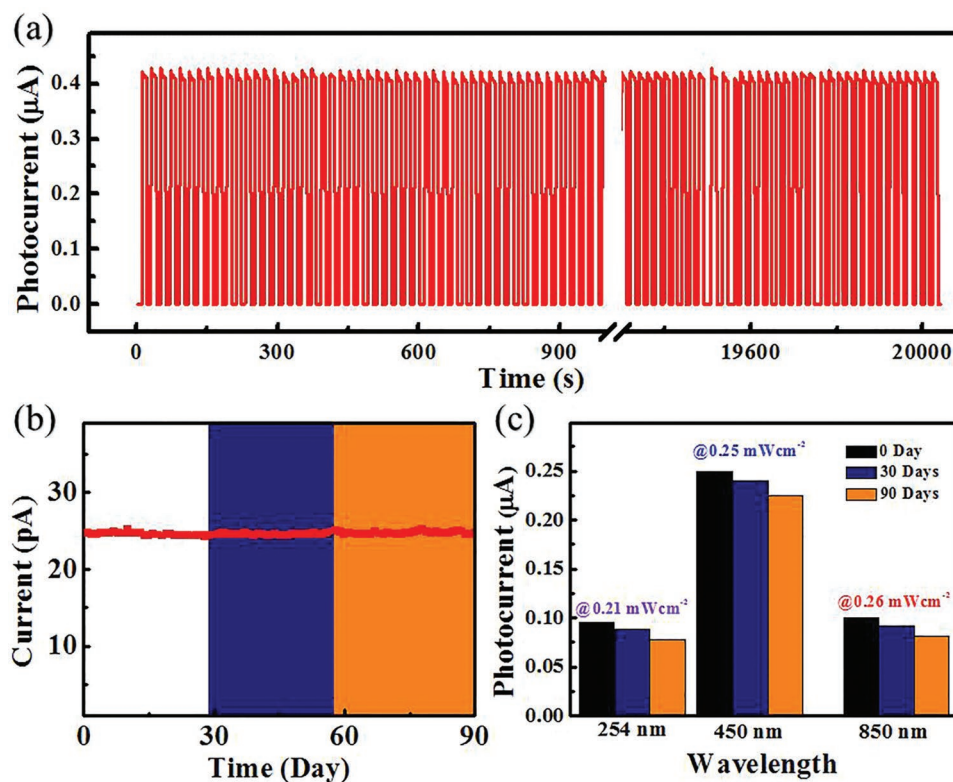


Figure 5. a) Time-dependent photoresponse of the device over 1000 cycles of operation at 3 V bias. Wavelength: 450 nm, the light intensity is 0.43 mW cm⁻². b,c) The evolution of dark current and photocurrent of the hybrid photodetector under 254, 450, and 850 nm illuminations in ambient conditions for varied durations.

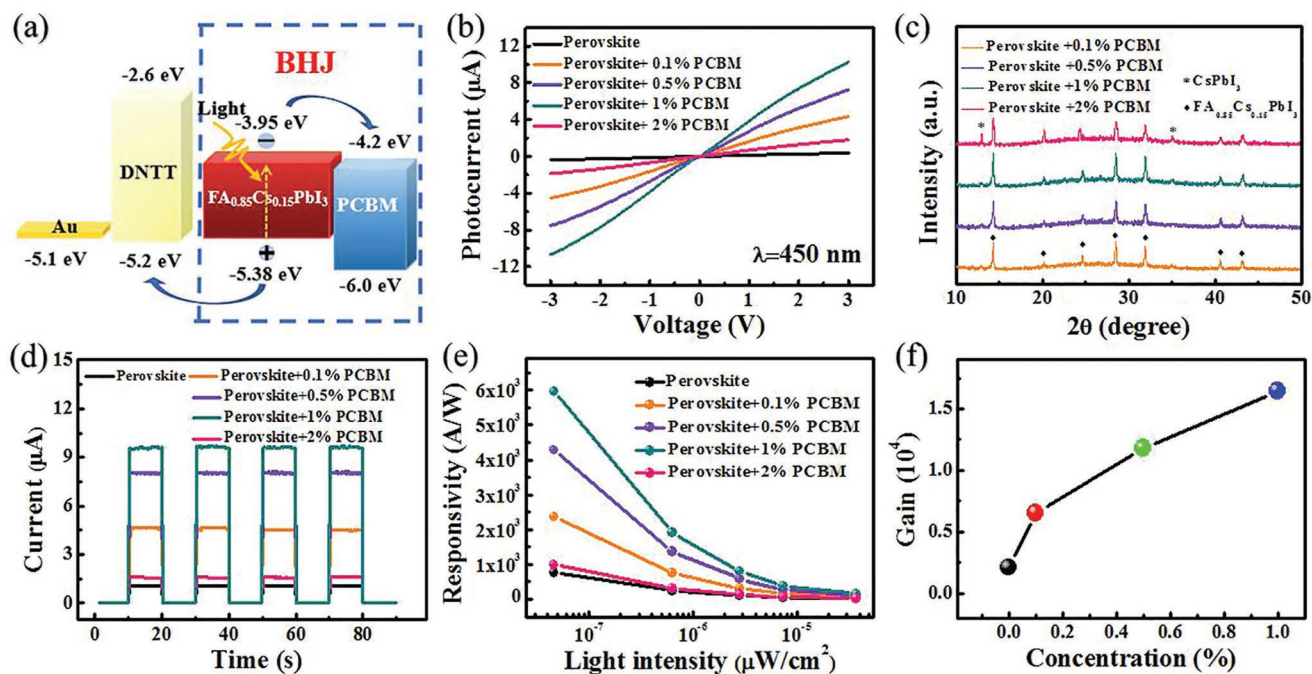


Figure 6. a) Energy band diagram of the perovskite-PCBM BHJ/DNTT heterostructure. b) *I*–*V* characteristics of perovskite-PCBM BHJ/DNTT-based detectors under 450 nm illumination (2.31 mW cm^{-2}) with different PCBM concentrations: 0, 0.1, 0.5, 1, and 2%. c) XRD pattern of perovskite-PCBM BHJ/DNTT films with different PCBM concentrations. d) Time-dependent photoresponse of the devices under 450 nm illumination (2.31 mW cm^{-2}). e) Responsivity as a function of light intensity for the perovskite-PCBM BHJ/DNTT heterostructure detectors with different PCBM concentrations. f) Gain of the samples with different PCBM concentrations ($\approx 46 \text{ nW cm}^{-2}$).

the perovskite, the existence of BHJs of perovskite and PCBM can facilitate the fast dissociation of excitons.^[55] Due to the decreased energy, electrons can be effectively transferred to the PCBM sites, which spatially separates electrons and holes and thus reduces their recombination. On the other hand, holes are readily transferred and extracted near the BHJ/DNTT interface and then continue to transport within the DNTT channel.

For comparison, five different concentrations of PCBM with weight ratios of 0 (without PCBM), 0.1, 0.5, 1, and 2% were studied (the detailed preparation procedures can be found in the Experimental Section).^[55] It was interesting to find that after doping with different amounts of PCBM, the five perovskite/DNTT and perovskite-PCBM BHJ/DNTT heterostructure detectors nearly had the same dark current (Figure S7, Supporting Information). Figure 6b compares the *I*–*V* characteristics of five perovskite/DNTT and perovskite-PCBM BHJ/DNTT heterostructures under illumination with 450 nm light. The photocurrent was only $\approx 1.0 \text{ } \mu\text{A}$ for the perovskite/DNTT-based device without doping. With the gradual addition of PCBM from 0.1 to 0.5%, the photoresponse significantly increased, which is understandable because an elevated concentration of PCBM can provide more sites for efficient trapping of electrons. The photocurrent increased to $\approx 10.0 \text{ } \mu\text{A}$ for perovskite-1% PCBM BHJ/DNTT-based devices, representing the highest value compared with that of other samples. However, further increasing the PCBM concentration to 2% led to severe degradation in the photocurrent. This could be explained by the change in the structure of FA_{0.85}Cs_{0.15}PbI₃ perovskite with excess PCBM addition. As shown in Figure 6c, in addition to the FA_{0.85}Cs_{0.15}PbI₃ phase, new diffraction peaks

attributable to CsPbI₃ perovskite appeared in the XRD pattern of the BHJ film with 2% PCBM. By comparing the time-dependent photoresponse of the hybrid photodetectors with different PCBM concentrations in Figure 6d, it can be found that all the devices exhibited prominent switching characteristics with a fast response speed and excellent reproducibility under periodically switched light illumination, and the variation of the photocurrent with PCBM concentration was consistent, according to the *I*–*V* curves shown in Figure 6b. The corresponding *R* values were calculated and plotted as a function of incident light intensity (Figure 6e). For all devices, the *R* values were found to decline with increasing light intensity due to recombination loss at a higher light intensity. Similar to the photocurrent, the *R* also depended strongly on the PCBM concentration: The value first increased gradually with the PCBM concentration changing from 0 to 1% and then declined significantly when increasing the PCBM concentration to 2%. At a low light intensity of $\approx 46 \text{ nW cm}^{-2}$, the *R* value reached $5.96 \times 10^3 \text{ A W}^{-1}$ for perovskite-1% PCBM BHJ/DNTT-based devices, which was nearly eight times higher than that of the hybrid photodetector without PCBM (759 A W^{-1}). The enhanced *R* values in samples with PCBM additives could be ascribed to the additional photoconductive gain (Figure 6f) due to the increased trapping time of electrons at PCBM sites, which is discussed later. In addition, the $i_{\text{on}}^{1/2}$ at 1 Hz bandwidth was calculated to be $\approx 1 \text{ pA Hz}^{-1/2}$ for the 1% PCBM device (Figure S8, Supporting Information), which is nearly identical to that of the detector without PCBM and implies that the PCBM addition did not influence the noise current of the hybrid photodetectors. Therefore, the *D**

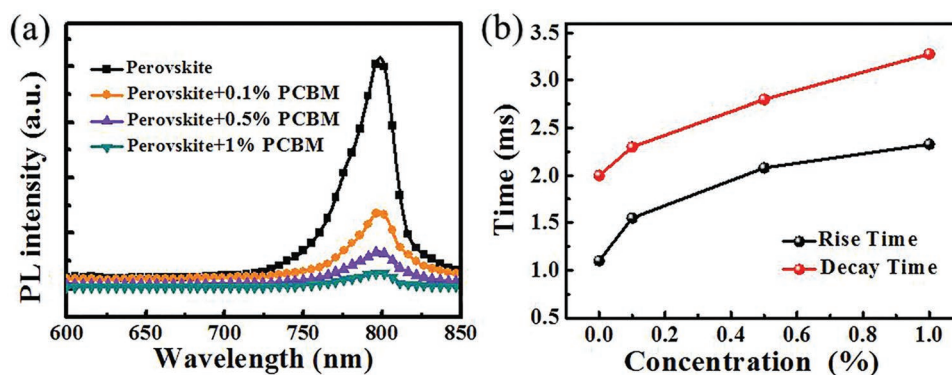


Figure 7. a) PL spectra of perovskite films doped with different amounts of PCBM. b) The rise/decay time of the perovskite-PCBM BHJ/DNTT films with different PCBM concentrations: 0, 0.1, 0.5, and 1%.

value was estimated to be as high as 7.96×10^{13} Jones for the perovskite-1% PCBM BHJ/DNTT hybrid detector.

To understand the selective electron trapping effect, PL measurements on the BHJs with different PCBM concentrations along with the pure perovskite film were conducted. As shown in Figure 7a, all the spectra had a nearly identical peak position and a similar spectral line shape, suggesting that the addition of PCBM did not alter the origin of the optical transition. However, the PL intensities varied significantly: The intensity values for BHJs with 0.1, 0.5, and 1% PCBM were only ≈ 33.5 , ≈ 15.9 , and $\approx 5.5\%$ of the pure perovskite film, respectively. Such a dramatic quenching of the PL intensity implies that a nonradiative kinetic process rather than radiative recombination began to dominate in the $\text{FA}_{0.85}\text{Cs}_{0.15}\text{PbI}_3$ perovskite with PCBM addition. In fact, photoexcited electrons in perovskite can quickly transfer to PCBM, whereas holes need to stay in the perovskite grains. Because of its low concentration, PCBM is likely to form discontinuous sites distributed uniformly in the BHJs. Such a distribution can lead to the trapping of electrons in PCBM sites and the spatial separation of photocarriers that can suppress their radiative recombination and extend the lifetimes of photocarriers. As a result, the BHJ of perovskite and PCBM was greatly beneficial for separating electrons and holes, which diminished radiative recombination loss and therefore enhanced the photoresponse. These results further confirm that hole transport in the DNTT layer dominated the photocurrent of the present hybrid photodetector as well.

Further device performance analysis revealed that the doping of PCBM can also influence the response speed. Figure S9 (Supporting Information) depicts the photoresponse of perovskite-PCBM BHJ/DNTT photodetectors with different PCBM doping concentrations, from which the corresponding rise/decay times of each device were determined and summarized in Figure 7b. It was observed that both rise and decay times slightly increased with increasing concentrations of PCBM additives. The increased rise time suggested that a longer duration was required to achieve an equilibrium state, which is characterized by equal rates of trapping and detrapping of electrons. Normally, during the electron trapping process, electrons tend to fill the trap states from deeper to shallower energy levels in the PCBM sites.^[8] Therefore, as the concentration of PCBM increases, more deep trap states are involved in the electron

trapping process. On the other hand, detrapping of electrons from deep trap states typically takes a longer time than that from shallow trap states.^[24,37] This explains the longer rise time observed for the detector with a higher PCBM concentration. In addition, for these devices, the longer decay time was attributed to the slower recombination of photoexcited electrons and holes after turning off the light illumination because electrons need to be released from the deep trap states in the PCBM sites. The slowest response speeds were calculated to be 2.33/3.28 ms (rise/decay times) for the perovskite-1% PCBM BHJ/DNTT-based device. Such a response is slower than for the device without PCBM doping but is comparable to, or even much faster than, those of previously reported hybrid photodetectors based on perovskite/OSCs, perovskite/graphene, and perovskite/2D TMDs (see Table 1).

3. Conclusion

In conclusion, we developed a high-performance and broadband photodetector based on a vertically stacked $\text{FA}_{0.85}\text{Cs}_{0.15}\text{PbI}_3$ perovskite/DNTT heterojunction. Due to the strong photogating effect, the as-fabricated hybrid detector exhibited a high responsivity of 778 A W^{-1} , a detectivity of 1.04×10^{13} Jones, and a gain of 2.1×10^3 . Furthermore, the device also displayed excellent stability and maintained nearly 80% of the initial photoresponse value after storage in air for 90 d. To further optimize the performance of the photodetector, PCBM was directly doped into the perovskite, which promoted electron-hole separation and provided electron accepting sites to selectively trap electrons. Further device analysis revealed that the as-doped perovskite-PCBM/DNTT hybrid photodetector displayed an improvement of nearly eight times in both the responsivity and specific detectivity over those of the device without PCBM doping.

4. Experimental Section

Material Preparation and Characterization: The $\text{FA}_{0.85}\text{Cs}_{0.15}\text{PbI}_3$ perovskite precursor was first prepared by dissolving 461 mg PbI_2 (Aldrich, 99%), 145 mg FAI (Xi'an Polymer Light Technology Cory, 99.5%), and 38.9 mg CsI (Aldrich, 99.9%) in a mixed solvent comprising 200 μL dimethyl sulfoxide (DMSO, Aldrich, >99.9%) and 800 μL N,N-dimethylformamide (DMF, Aldrich, 99.8%). The

as-prepared solution was then stirred at 70 °C overnight prior to use. The $\text{FA}_{0.85}\text{Cs}_{0.15}\text{PbI}_3$ film was fabricated by spin-coating 60 μL of the above precursor onto a clean glass substrate at 600 rpm for 10 s, cleansing with antisolvent 20 μL ethyl acetate, spinning at 2000 rpm for another 20 s, and finally annealing at 135 °C for 15 min. To synthesize the perovskite-PCBM BHJ films, PCBM solutions with different concentrations were first obtained by dissolving different amounts of PCBM (Xi'an Polymer Light Technology Corp, 99.5%) into a chlorobenzene solvent. Then, 10 μL of PCBM chlorobenzene solutions with different concentrations were separately mixed with 1 mL $\text{FA}_{0.85}\text{Cs}_{0.15}\text{PbI}_3$ perovskite precursor solution to obtain BHJ precursor solutions with different PCBM weight ratios of 0.1, 0.5, 1, and 2% relative to perovskite. For comparison, 10 μL chlorobenzene without PCBM was also incorporated into the perovskite precursor solution for preparing the control device. The BHJ precursor solutions were spin-coated onto a clean glass substrate at 600 rpm for 10 s and then 1600 rpm for 20 s. During the spin-coating, 20 μL ethyl acetate acting as antisolvent was dropped onto the substrate. Afterward, the sample was annealed at 100 °C for 15 min, followed by annealing at 70 °C for 20 min and 100 °C for 10 min to remove residual solvent. The morphology of the as-prepared films was characterized by a FESEM (Hitachi, SU8020). The optical absorption spectra were recorded using a UV-vis spectrophotometer (UV-2550, Shimadzu, Japan). The phase composition of the samples was studied using an X-ray diffractometer (Rigaku D/max-rB). A confocal laser Raman spectrometer (Horiba Jobin Yvon, Labram HR evolution) was employed to record the PL spectra.

Device Fabrication and Analysis: To fabricate the hybrid photodetectors, thin films of $\text{FA}_{0.85}\text{Cs}_{0.15}\text{PbI}_3$ perovskite or $\text{FA}_{0.85}\text{Cs}_{0.15}\text{PbI}_3$ perovskite-PCBM BHJ were first prepared on a cleaned SiO_2 (300 nm)/Si substrate, followed by thermal evaporation of DNTT film to form a vertically stacked heterostructure. Afterward, Au source/drain electrodes with a thickness of ≈ 50 nm were fabricated via an electron-beam evaporator through a shadow mask with a channel width of 18 μm . The electrical measurements were conducted with a semiconductor characterization system (4200-SCS, Keithley Co. Ltd.), equipped with a monochromator (SP 2150, Princeton Co.). To study the optoelectronic properties, laser diodes (Tanon Company, UV-100) with different wavelengths (254, 450, and 850 nm) were adopted. The power intensity of the light sources was carefully calibrated by a power meter (Thorlabs GmbH, PM 100D) before measurement. For the response speed study, the device was illuminated with a laser diode driven by a high-frequency signal generator, and the pulsed voltage was recorded by an oscilloscope (Tektronix, TDS2012B). Unless otherwise specified, all measurements were performed in air at room temperature.

Supporting Information

Supporting Information is available from the Wiley Online Library or from the author.

Acknowledgements

This work was supported by the National Natural Science Foundation of China (NSFC, Nos. 61575059, 61675062, and 21501038), the Fundamental Research Funds for the Central Universities (JZ2018HGPB0275, JZ2018HGXC0001, and JZ2018HGTA0220), and the Open Foundation of Anhui Provincial Key Laboratory of Advanced Functional Materials and Devices (4500-411104/011).

Conflict of Interest

The authors declare no conflict of interest.

Keywords

hybrid structures, organic semiconductors, perovskite materials, phototransistors, photogating effect

Received: February 15, 2019

Revised: April 8, 2019

Published online:

- [1] H. Zhou, Q. Chen, G. Li, S. Luo, T. B. Song, H. S. Duan, Z. Hong, J. You, Y. Liu, Y. Yang, *Science* **2014**, 345, 542.
- [2] Q. Tai, P. You, H. Sang, Z. Liu, C. Hu, H. L. W. Chan, F. Yan, *Nat. Commun.* **2016**, 7, 11105.
- [3] Y. Ling, Z. Yuan, Y. Tian, X. Wang, J. C. Wang, Y. Xin, K. Hanson, B. Ma, H. Gao, *Adv. Mater.* **2016**, 28, 305.
- [4] W. Deng, X. Xu, X. Zhang, Y. Zhang, X. Jin, L. Wang, S. T. Lee, J. Jie, *Adv. Funct. Mater.* **2016**, 26, 4797.
- [5] X. Hu, X. Zhang, L. Liang, J. Bao, S. Li, W. Yang, Y. Xie, *Adv. Funct. Mater.* **2014**, 24, 7373.
- [6] L. Dou, Y. Yang, J. You, Z. Hong, W. H. Chang, G. Li, Y. Yang, *Nat. Commun.* **2014**, 5, 5404.
- [7] W. Deng, X. Zhang, L. Huang, X. Xu, L. Wang, J. Wang, Q. Shang, S. T. Lee, J. Jie, *Adv. Mater.* **2016**, 28, 2201.
- [8] C. Xie, P. You, Z. Liu, L. Li, F. Yan, *Light: Sci. Appl.* **2017**, 6, e17023.
- [9] H. Zhu, Y. Fu, F. Meng, X. Wu, Z. Gong, Q. Ding, M. V. Gustafsson, M. T. Trinh, S. Jin, X.-Y. Zhu, *Nat. Mater.* **2015**, 14, 636.
- [10] Y. Fu, H. Zhu, A. W. Schrader, D. Liang, Q. Ding, P. Joshi, L. Hwang, X. Y. Zhu, S. Jin, *Nano Lett.* **2016**, 16, 1000.
- [11] J. Y. Han, J. Wang, M. Yang, X. Kong, X. Q. Chen, Z. H. Huang, H. Guo, J. Gou, S. L. Tao, Z. J. Liu, Z. M. Wu, Y. D. Jiang, *Adv. Mater.* **2018**, 30, 1804020.
- [12] M. Ahmadi, T. Wu, B. Hu, *Adv. Mater.* **2017**, 29, 1605242.
- [13] J. Zhou, J. Huang, *Adv. Sci.* **2018**, 5, 1700256.
- [14] W. Tian, H. Zhou, L. Li, *Small* **2017**, 13, 1702107.
- [15] H. Lu, W. Tian, F. Cao, Y. Ma, B. Gu, L. Li, *Adv. Funct. Mater.* **2016**, 26, 1296.
- [16] Q. Lin, A. Armin, D. M. Lyons, P. L. Burn, P. Meredith, *Adv. Mater.* **2015**, 27, 2060.
- [17] F. Li, C. Ma, H. Wang, W. Hu, W. Yu, A. D. Sheikh, T. Wu, *Nat. Commun.* **2015**, 6, 8238.
- [18] Y. Guo, C. Liu, H. Tanaka, E. Nakamura, *J. Phys. Chem. Lett.* **2015**, 6, 535.
- [19] T. S. Sherkar, C. Momblona, L. Gil-Escrig, J. Ávila, M. Sessolo, H. J. Bolink, L. J. A. Koster, *ACS Energy Lett.* **2017**, 2, 1214.
- [20] J.-W. Lee, S.-H. Bae, N. De Marco, Y.-T. Hsieh, Z. Dai, Y. Yang, *Mater. Today Energy* **2018**, 7, 149.
- [21] Y. Lee, J. Kwon, E. Hwang, C.-H. Ra, W. J. Yoo, J.-H. Ahn, J. H. Park, J. H. Cho, *Adv. Mater.* **2015**, 27, 41.
- [22] Z. Sun, L. Aigouy, Z. Chen, *Nanoscale* **2016**, 8, 7377.
- [23] Y. Wang, Y. Zhang, Y. Lu, W. Xu, H. Mu, C. Chen, H. Qiao, J. Song, S. Li, B. Sun, Y.-B. Cheng, Q. Bao, *Adv. Opt. Mater.* **2015**, 3, 1389.
- [24] Y. Shao, Y. Liu, X. Chen, C. Chen, I. Sarpkaya, Z. Chen, Y. Fang, J. Kong, K. Watanabe, T. Taniguchi, A. Taylor, J. Huang, F. Xia, *Nano Lett.* **2017**, 17, 7330.
- [25] L. Qian, Y. Sun, M. Wu, D. Xie, L. Ding, G. Shi, *Adv. Mater.* **2017**, 29, 1606175.
- [26] F. Li, H. Wang, D. Kufer, L. Liang, W. Yu, E. Alarousu, C. Ma, Y. Li, Z. Liu, C. Liu, N. Wei, F. Wang, L. Chen, O. F. Mohammed, A. Fratalocchi, X. Liu, G. Konstantatos, T. Wu, *Adv. Mater.* **2017**, 29, 1602432.
- [27] X. Li, D. Yu, J. Chen, Y. Wang, F. Cao, Y. Wei, Y. Wu, L. Wang, Y. Zhu, Z. Sun, J. Ji, Y. Shen, H. Sun, H. Zeng, *ACS Nano* **2017**, 11, 2015.

- [28] D.-H. Kang, S. R. Pae, J. Shim, G. Yoo, J. Jeon, J. W. Leem, J. S. Yu, S. Lee, B. Shin, J.-H. Park, *Adv. Mater.* **2016**, 28, 7799.
- [29] Y. Wang, R. Fullon, M. Acerce, C. E. Petoukhoff, J. Yang, C. Chen, S. Du, S. K. Lai, S. P. Lau, D. Voiry, D. O'Carroll, G. Gupta, A. D. Mohite, S. Zhang, H. Zhou, M. Chhowalla, *Adv. Mater.* **2017**, 29, 1603995.
- [30] C. Ma, Y. Shi, W. Hu, M. H. Chiu, Z. Liu, A. Bera, F. Li, H. Wang, L. J. Li, T. Wu, *Adv. Mater.* **2016**, 28, 3683.
- [31] J. Lu, A. Carvalho, H. Liu, S. X. Lim, A. H. Castro Neto, C. H. Sow, *Angew. Chem., Int. Ed.* **2016**, 55, 11945.
- [32] C. Xie, F. Yan, *Small* **2017**, 13, 1701822.
- [33] S. Chen, C. Teng, M. Zhang, Y. Li, D. Xie, G. Shi, *Adv. Mater.* **2016**, 28, 5969.
- [34] S. Tong, J. Sun, C. Wang, Y. Huang, C. Zhang, J. Shen, H. Xie, D. Niu, S. Xiao, Y. Yuan, J. He, J. Yang, Y. Gao, *Adv. Electron. Mater.* **2017**, 3, 1700058.
- [35] Y. Chen, Y. Chu, X. Wu, W. Ou-Yang, J. Huang, *Adv. Mater.* **2017**, 29, 1704062.
- [36] C. Xie, Y. Wang, Z. X. Zhang, D. Wang, L. B. Luo, *Nano Today* **2018**, 19, 41.
- [37] L. Qin, L. Wu, B. Kattel, C. Li, Y. Zhang, Y. Hou, J. Wu, W.-L. Chan, *Adv. Funct. Mater.* **2017**, 27, 1704173.
- [38] C. Liu, H. Peng, K. Wang, C. Wei, Z. Wang, X. Gong, *Nano Energy* **2016**, 30, 27.
- [39] X. Zhang, Q. Wang, Z. Jin, J. Zhang, S. (Frank) Liu, *Nanoscale* **2017**, 9, 6278.
- [40] W. Chen, J. Hao, W. Hu, Z. Zang, X. Tang, L. Fang, T. Niu, M. Zhou, *Small* **2017**, 13, 1604085.
- [41] J. Milvich, T. Zaki, M. Aghamohammadi, R. Rödel, U. Kraft, H. Klauk, J. N. Burghartz, *Org. Electron.* **2015**, 20, 63.
- [42] F. X. Liang, J. Z. Wang, Z. X. Zhang, Y. Y. Wang, Y. Gao, L. B. Luo, *Adv. Opt. Mater.* **2017**, 5, 1700654.
- [43] K. Galkowski, A. Mitoglu, A. Miyata, P. Plochocka, O. Portugall, G. E. Eperon, J. T.-W. Wang, T. Stergiopoulos, S. D. Stranks, H. J. Snaith, R. J. Nicholas, *Energy Environ. Sci.* **2016**, 9, 962.
- [44] G. Konstantatos, M. Badioli, L. Gaudreau, J. Osmond, M. Bernechea, F. P. G. de Arquer, F. Gatti, F. H. L. Koppens, *Nat. Nanotechnol.* **2012**, 7, 363.
- [45] C. Xie, C. Mak, X. Tao, F. Yan, *Adv. Funct. Mater.* **2017**, 27, 1603886.
- [46] R. Zhuo, L. Zeng, H. Yuan, D. Wu, Y. Wang, Z. Shi, T. Xu, Y. Tian, X. Li, Y. H. Tsang, *Nano Res.* **2019**, 12, 183.
- [47] L. H. Zeng, M. Z. Wang, H. Hu, B. Nie, Y. Q. Yu, C. Y. Wu, L. Wang, J. G. Hu, C. Xie, F. X. Liang, L. B. Luo, *ACS Appl. Mater. Interfaces* **2013**, 5, 9362.
- [48] Z. X. Zhang, L. H. Zeng, X. W. Tong, Y. Gao, C. Xie, Y. H. Tsang, L. B. Luo, Y. C. Wu, *J. Phys. Chem. Lett.* **2018**, 9, 1185.
- [49] C. Xie, F. Yan, *ACS Appl. Mater. Interfaces* **2017**, 9, 1569.
- [50] L. Wang, J. Jie, Z. Shao, Q. Zhang, X. Zhang, Y. Wang, Z. Sun, S. T. Lee, *Adv. Funct. Mater.* **2015**, 25, 2910.
- [51] Q. Lin, A. Armin, P. L. Burn, P. Meredith, *Laser Photonics Rev.* **2016**, 10, 1047.
- [52] D. Wu, Y. Wang, L. Zeng, C. Jia, E. Wu, T. Xu, Z. Shi, Y. Tian, X. Li, Y. H. Tsang, *ACS Photonics* **2018**, 5, 3820.
- [53] Z. Song, A. Abate, S. C. Watthage, G. K. Liyanage, A. B. Phillips, U. Steiner, M. Graetzel, M. J. Heben, *Adv. Energy Mater.* **2016**, 6, 1600846.
- [54] C. H. Chiang, C. G. Wu, *Nat. Photonics* **2016**, 10, 196.
- [55] J. Xu, A. Buin, A. H. Ip, W. Li, O. Voznyy, R. Comin, M. Yuan, S. Jeon, Z. Ning, J. J. McDowell, P. Kanjanaboos, J.-P. Sun, X. Lan, L. N. Quan, D. H. Kim, I. G. Hill, P. Maksymovych, E. H. Sargent, *Nat. Commun.* **2015**, 6, 7081.